Assessment of the pseudo-tracking approach for the calculation of material acceleration and pressure fields from time-resolved PIV
Part II. Spatio-temporal filtering

Van Gent, P. L.; Schrijer, F. F.J.; Van Oudheusden, B. W.

DOI
10.1088/1361-6501/aaab84

Publication date
2018

Document Version
Final published version

Published in
Measurement Science and Technology

Assessment of the pseudo-tracking approach for the calculation of material acceleration and pressure fields from time-resolved PIV: part II. Spatio-temporal filtering

IOP Publishing Measurement Science and Technology
Meas. Sci. Technol. **29** (2018) 045206 (18pp) https://doi.org/10.1088/1361-6501/aaab84

Assessment of the pseudo-tracking approach for the calculation of material acceleration and pressure fields from time-resolved PIV: part II. Spatio-temporal filtering

P L van Gent, F F J Schrijer and B W van Oudheusden

Faculty of Aerospace Engineering, Delft University of Technology, Netherlands

E-mail: p.l.vangent@tudelft.nl

Received 3 October 2017, revised 16 January 2018
Accepted for publication 30 January 2018
Published 9 March 2018

Abstract

The present study characterises the spatio-temporal filtering associated with pseudo-tracking. A combined theoretical and numerical assessment is performed that uses the relatively simple flow case of a two-dimensional Taylor vortex as analytical test case. An additional experimental assessment considers the more complex flow of a low-speed axisymmetric base flow, for which time-resolved tomographic PIV measurements and microphone measurements were obtained. The results of these assessments show how filtering along Lagrangian tracks leads to amplitude modulation of flow structures. A cut-off track length and spatial resolution are specified to support future applications of the pseudo-tracking approach. The experimental results show a fair agreement between PIV and microphone pressure data in terms of fluctuation levels and pressure frequency spectra. The coherence and correlation between microphone and PIV pressure measurements were found to be substantial and almost independent of the track length, indicating that the low-frequency behaviour of the flow could be reproduced regardless of the track length. It is suggested that a spectral analysis can be used inform the selection of a suitable track length and to estimate the local error margin of reconstructed pressure values.

Keywords: PIV, pseudo-tracking, material acceleration, pressure, microphone

(Some figures may appear in colour only in the online journal)

1. Introduction

Pseudo-tracking refers to the construction of imaginary particle paths from PIV velocity fields and the subsequent estimation of the particle (material) acceleration at the initial particle position (Jensen *et al* 2003, Liu and Katz 2006). By virtue of the momentum equation, pressure fields can subsequently be obtained by spatial integration. The present study is part of a wider assessment of the performance of the method. Part I of the study focusses on the propagation of measurement errors and numerical error sources (van Gent *et al* 2018). The reader is referred to that article for more background to the study and a detailed description of the working principle of pseudo-tracking.

Earlier assessments of pseudo-tracking focussed on determining the optimal spatial and temporal resolutions for which the overall (combined) error in the reconstructed pressure fields is minimum (Jensen and Pedersen 2004, Violato *et al* 2011, de Kat and van Oudheusden 2012, van Oudheusden 2013, Laskari *et al* 2016, McClure and Yarusevych 2017). In addition, de Kat and van Oudheusden (2012) recommended minimum spatial and temporal resolutions with respect to

the flow length and time scales. Notwithstanding the valuable insights that earlier assessment have provided, the exact mechanism by which the temporal filtering that occurs along Lagrangian tracks leads to spatial filtering of flow structures viewed in a Eulerian perspective, has so far not been described.

The present article therefore investigates the spatio-temporal filtering behaviour of the pseudo-tracking method. Specific attention is given to the impact of spatio-temporal filtering on power spectra of pressure fluctuations as such spectra are widely used in the analysis of dynamically evolving flows.

To allow making general conclusions, the generic flow case of a two-dimensional Taylor vortex is used as a basis for a theoretical analysis. A two-dimensional vortex was also considered in previous assessments (Charonko *et al* 2010, de Kat and van Oudheusden 2012, McClure and Yarusevych 2017). The present investigation, however, takes a different and more theoretical approach. In addition to the relatively simple case of a two-dimensional vortex, the performance of pseudo-tracking is characterised using the more complex flow case of a low-speed flow over an axisymmetric body, for which time-resolved PIV measurements have been obtained. The use of an experimental test case is motivated by the need to obtain pressure spectra (which are challenging to obtain from numerical simulations) and the desire to demonstrate the capabilities of pseudo-tracking under realistic measurement conditions. The choice of the particular flow case is motivated by its richness in terms of spatial and temporal flow scales, its challenging nature that is inherent to three-dimensional separating-reattaching flows and its relevance in the field of launcher aerodynamics.

The structure of this article is as follows. Section 2 contains a theoretical/numerical assessment. Section 3 presents the experimental arrangements and data processing for the experimental assessment after which section 4 discusses the experimental results. Section 5 proposes a method to inform the selection of a suitable track length as well as to estimate the local error margin of PIV-based pressure values. The proposed method makes use of experimental data only and does not require the availability of any reference data. Finally, section 6 presents the conclusions.

2. Theoretical/numerical analysis

The present section investigates the spatio-temporal filtering associated with pseudo-tracking by means of a combined theoretical/numerical assessment. Section 2.1 describes the filter behaviour from a Lagrangian perspective. The filter behaviour observed from a Eulerian perspective is investigated in section 2.2 by considering a stationary vortex. The impact of PIV resolution is discussed in section 2.3. Section 2.4 describes the combined impact of temporal and spatial resolution. The case of a moving vortex is discussed in section 2.5.

2.1. Filter behaviour from a Lagrangian perspective

The filter behaviour from a Lagrangian perspective can be expressed in terms of transfer functions that reflect the amplitude modulation at different frequencies (e.g. Foucaut and Stanislas (2002)). The total transfer function for pseudo-tracking is a combination of the transfer functions of the PIV measurement (T_{piv}), the track construction procedure (T_{track}) and the determination of the derivative from track velocities (T_{diff}):

$$T_{\mathrm{Lag}} = T_{\mathrm{piv}} \times T_{\mathrm{track}} \times T_{\mathrm{diff}} = \mathrm{sinc}\left(\frac{\Delta t_{\mathrm{piv}}}{\lambda_t}\right) \times \frac{\pi \Delta t_{\mathrm{piv}}}{\lambda_t} \cot\left(\frac{\pi \Delta t_{\mathrm{piv}}}{\lambda_t}\right) \times T_{\mathrm{diff}}. \quad (1)$$

Here Δt_{piv} is the time separation between PIV velocity fields and λ_t is the Lagrangian time scale. Throughout this paper $\mathrm{sinc}(x) = \sin(\pi x)/(\pi x)$ represents the normalised cardinal sine function. The transfer function for PIV (T_{piv}) is defined based on central differencing (of particle location) with a time step of $\Delta t_{\mathrm{piv}}/2$, which is illustrative for separated flows (Lynch *et al* 2014). The transfer function for the track construction (T_{track}) is based on trapezoidal integration with a time step that is equal to Δt_{piv} (Butz 2015). The transfer function for the determination of the derivative of the track velocity (T_{diff}) depends on the numerical approach used (see van Gent *et al* (2018), section 2 for an overview). For central differencing (CD) with a time step $\Delta T = n_{\mathrm{piv}} \Delta t_{\mathrm{piv}}$, the transfer function is $T_{\mathrm{CD}} = \mathrm{sinc}(2\Delta T/\lambda_t)$ (see e.g. Foucaut and Stanislas (2002)). Here, n_{piv} is the number of PIV velocity fields in a single integration direction, e.g. $n_{\mathrm{piv}} = 3$ for a track that covers 7 velocity fields. The transfer functions for first-order least-square fitting (LS), $T_{\mathrm{LS}} = \sum_i^{n_{\mathrm{piv}}} (2i\sin(\mathrm{i}\omega\Delta t_{\mathrm{piv}}))/\sum_i^{n_{\mathrm{piv}}} (2i^2\omega\Delta t_{\mathrm{piv}})$, and third-order least square fitting (3LS) can be derived using the convolution coefficients for the first derivative in Savinsky–Golay tables (e.g. Gorry (1990)). Note that $\omega = 2\pi/\lambda_t$ is the angular velocity. Figure 1 shows the transfer functions for the different methods for track lengths up to the Nyquist frequency.

The figure shows that all methods (CD, LS, 3LS) act as low-pass filters. The cut-off frequency decreases for longer tracks and lower-order methods. In effect, a lower cut-off frequency acts as to filter out more high-frequency noise and possibly more flow time scales of the flow, leading to a reduction in propagation of random velocity errors and a possible increase in truncation error. The transfer functions for CD and LS are identical for $n_{\mathrm{piv}} = 1$. For longer tracks ($n_{\mathrm{piv}} > 1$), the transfer functions for CD and LS are rather similar. The cut-off frequency based of a threshold of -3 dB for 3LS is about twice as high as the cut-off frequencies for CD and LS for a given track length (n_{piv}). For a given cut-off frequency, the roll-off for 3LS is more pronounced than for CD and LS. Further, the figure shows that for $n_{\mathrm{piv}} > 1$ the combined transfer function of PIV, track construction and CD/LS is dominated by the latter.

In addition to from amplitude modulation, the frequency response includes a phase shift if the methods are not implemented symmetrically around a centre time instance, as is the case for tracks that start from positions near the boundaries of the measurement domain.

2.2. Filter behaviour from a Eulerian perspective

The filter behaviour observed from a Eulerian perspective depends on the characteristics of the flow field and is analysed

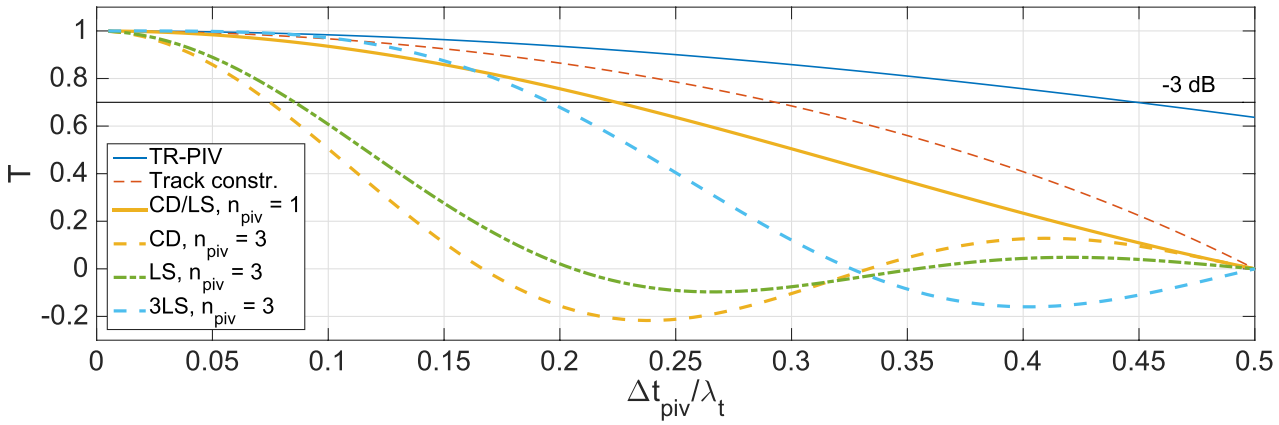

Figure 1. Transfer functions from a Lagrangian perspective.

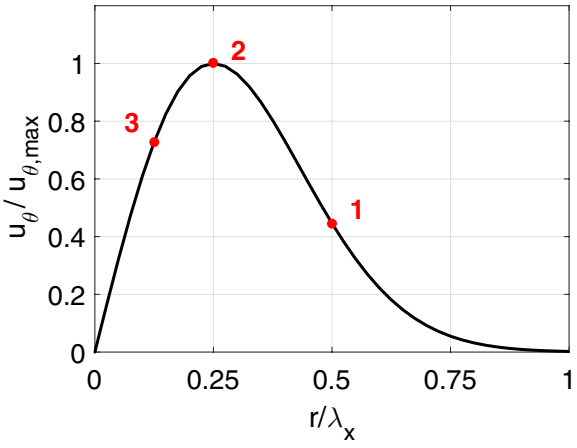

Figure 2. Tangential velocity.

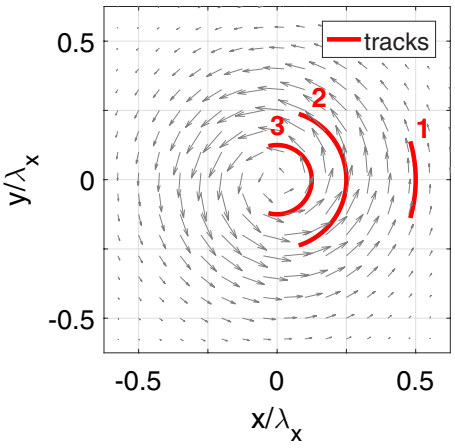

Figure 3. Vortex with tracks starting from different initial positions.

using the generic flow case of a two-dimensional Taylor vortex (see introduction for details on the choice of the flow case). The present section considers the case of a stationary vortex. The vortex is initially sampled so that any associated spatial filtering can be neglected with respect to the impact of Lagrangian filtering from pseudo-tracking.

Equations (2)–(4) express the velocity, material acceleration in radial direction and pressure distributions of a Taylor vortex, respectively. Equations (2) and (4) are defined based on Panton (1996) and Charonko *et al* (2010)). Equation (3) has been derived by considering that a vortex represents a circular motion so that $Du/Dt|_r = u_\theta(r)^2/r$.

$$u_\theta(r) = \frac{H}{8\pi}\frac{r}{\nu t^{*2}}\exp\left(-\frac{r^2}{4\nu t^*}\right) \tag{2}$$

$$\left.\frac{Du}{Dt}\right|_r(r) = \frac{H^2}{64\pi^2}\frac{r}{\nu^2 t^{*4}}\exp\left(-\frac{r^2}{2\nu t^*}\right) \tag{3}$$

$$p(r) = -\frac{\rho H^2}{64\pi^2\nu t^{*3}}\exp\left(-\frac{r^2}{2\nu t^*}\right) + p_\infty \tag{4}$$

Here, u_θ is the tangential velocity, r is the radial position, H is the vortex angular momentum, ρ is the density, ν is the kinematic viscosity, t^* is the time and p_∞ is the freestream pressure far away from the vortex core. Similarly to Charonko *et al* (2010), the angular momentum is taken as $H = 1 \times 10^6$ m^2, the density as $\rho = 1000$ kg m^3, and the viscosity as $\nu = 1 \times 10^6$ m^2 s^1. The freestream pressure p_∞ is set at 1×10^5 Pa.

$u_{\theta,\max}$ is the maximum tangential velocity, used to non-dimensionalise the vortex velocity distribution. For the purpose of normalisation, the reference length scale λ_x is defined as twice distance from between the maxima in tangential velocity along a symmetry line (i.e. $u_\theta(\lambda_x/4) = u_{\theta,\max}$). $\lambda_{\text{turn}}(r)$ is the turnover rate and λ_t is the reference time scale defined as the turnover rate at the distance from the core where the tangential velocity is maximum (i.e. $\lambda_{\text{turn}}(\lambda_x/4)$). It is assumed that the decay rate of the vortex is small compared to the observation time so that for the purpose of the analysis, the size and structure of the vortex remain constant. Mathematically this is achieved by keeping the time (t^*) constant. Due to the normalisation used, the results presented below are independent on the value of t^*.

Figure 2 shows the tangential velocity as a function of distance from the vortex core. To illustrate the filter behaviour of pseudo-tracking, Lagrangian paths are calculated taking three sample locations along the horizontal symmetry line as initial positions. Point 1 is located far from the core ($x/\lambda_x = 0.5$). Point 2 is located at the radius of maximum tangential velocity ($x/\lambda_x = 0.25$), and point 3 lies close to the core ($x/\lambda_x = 0.125$), see figures 2 and 3).

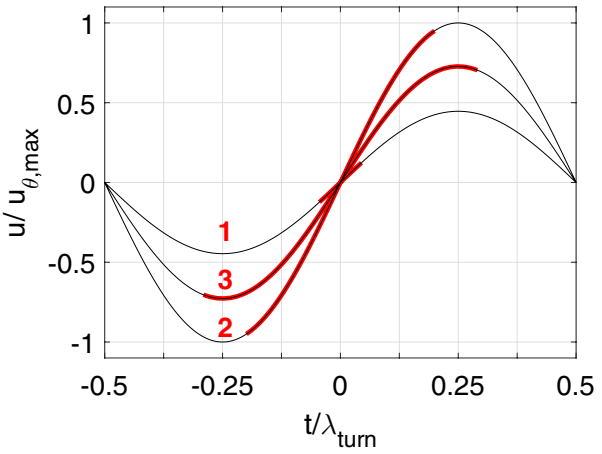

Figure 4. Streamwise velocity along track as a function of normalised time.

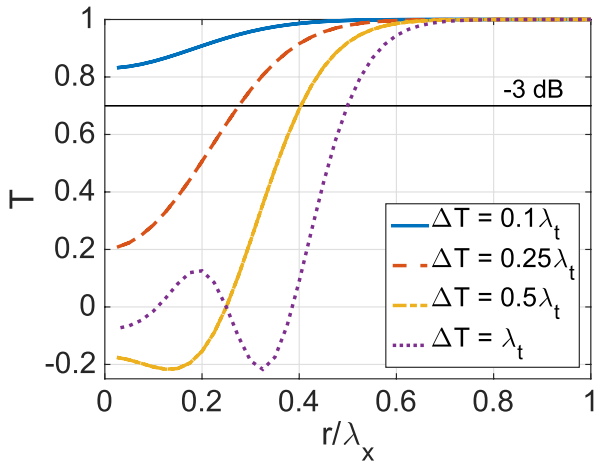

Figure 5. Transfer function for central differencing for different temporal track lengths.

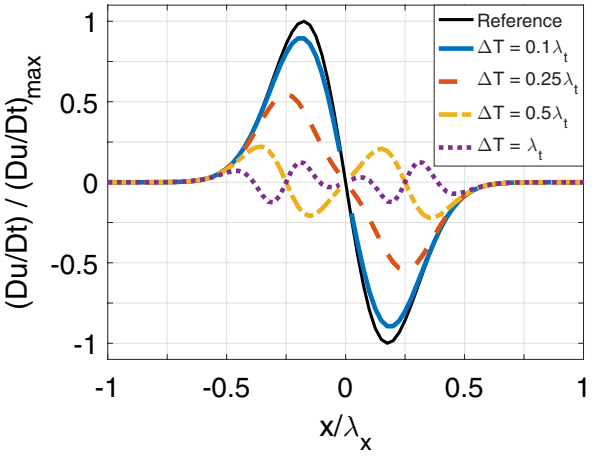

Figure 6. Material acceleration at $y = 0$ for different temporal track lengths.

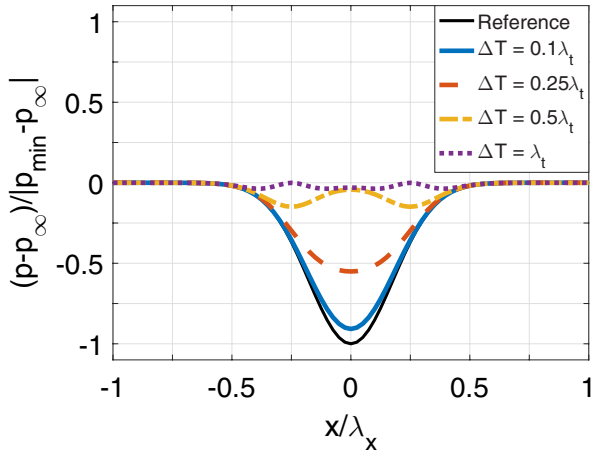

Figure 7. Pressure at $y = 0$ for different temporal track lengths.

Considering the equations for circular motions, the u- and v- velocity along the particle paths follow a sine or cosine function, respectively, with an amplitude $u_\theta(r)$ and a period $\lambda_{\text{turn}} = 2\pi r/u_\theta(r)$. This is illustrated in figure 4, which shows the u-velocity as a function of time for the different tracks. Note that the time is normalised by the turnover time $\lambda_{\text{turn}}(r)$, which decreases towards the core. The figure shows that for similar temporal track lengths (indicated in red), tracks closer to the core will cover larger parts of their respective turnover times. As a consequence, the impact of temporal filtering during differentiation of track velocity (i.e. determination of the material acceleration) increases towards the core (compare figure 1). This also becomes clear when expressing the transfer functions from section 2.1 as functions of the distance from the core e.g. for central differencing $T_{\text{Eul,CD}} = \text{sinc}(2\Delta T/\lambda_{\text{turn}}) = \text{sinc}(u_\theta \Delta T/\pi r)$. From the resulting transfer functions it is apparent that the modulation increases towards the core and with temporal track length (see figure 5).

Figure 6 shows the material acceleration in streamwise direction at $y = 0$ for different track lengths. The results from pseudo-tracking can be obtained by multiplying the reference material acceleration with the transfer function for central differencing from figure 5 i.e. $Du/Dt|_{\text{pseu.tra.}} = Du/Dt|_{\text{ref}} \times T_{\text{Eul,CD}} = u_\theta \Delta T^{-1} \sin(u_\theta \Delta \text{Tr}^{-1})$. This outcome has been verified by comparison with results obtained by applying pseudo-tracking to the velocity data. Figure 6 shows that for relatively short track lengths, the reconstructed material accelerations remain close to the reference values. As the track length increases, the absolute value of the maxima decreases and the distance between the two extrema increases. For track lengths above $\Delta T > 0.3\lambda_t$, additional extrema occur due to oscillations in the transfer function (compare figure 5). Other numerical differentiation techniques that have less pronounced oscillations than CD (such as LS, see figure 1), can be expected to perform better in this respect.

Figure 7 shows the pressure distributions calculated upon solving the momentum equation (see van Gent *et al* (2018); section 2). Neumann boundary conditions are implicitly imposed on all sides except for one corner point, where the reference pressure is prescribed as a Dirichlet boundary condition. It can readily be verified that the spatial derivative of the pressure distribution (which is similar to a cosine) results in the distribution of the material acceleration (which is similar to a sine). Like for the acceleration, the peak response decreases with increasing track lengths and additional extrema occur for $\Delta T > 0.3\lambda_t$.

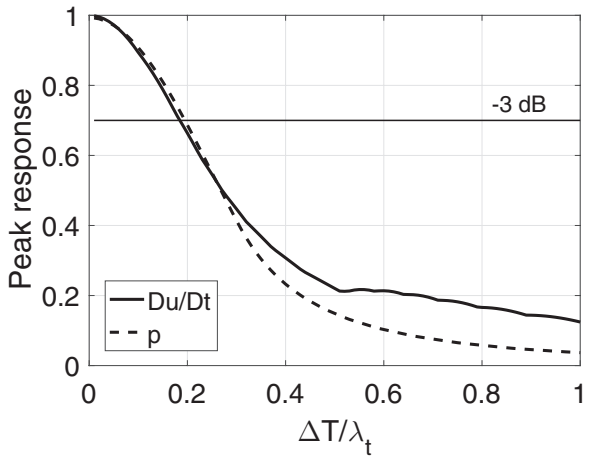

Figure 8. Peak response as function of temporal track length.

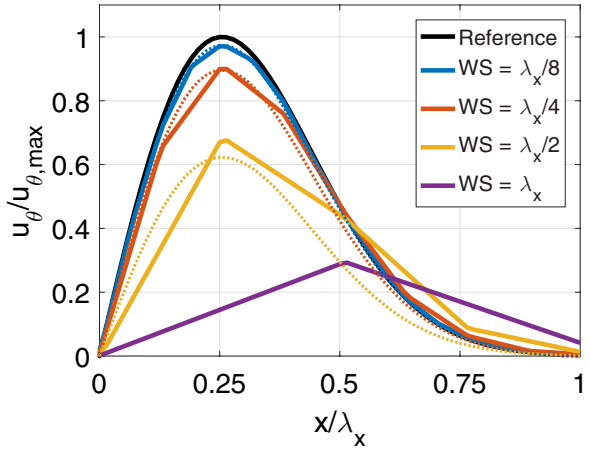

Figure 9. Tangential velocity at $y = 0$ for different spatial resolutions; numerical (solid) and theoretical (dotted) results.

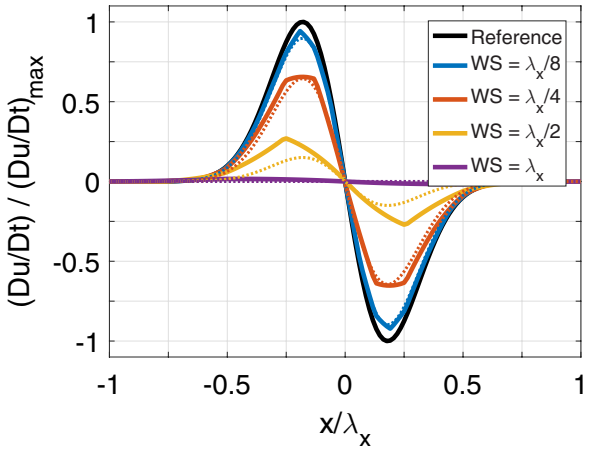

Figure 10. Material acceleration at $y = 0$ for different spatial resolutions; numerical (solid) and theoretical (dotted) results.

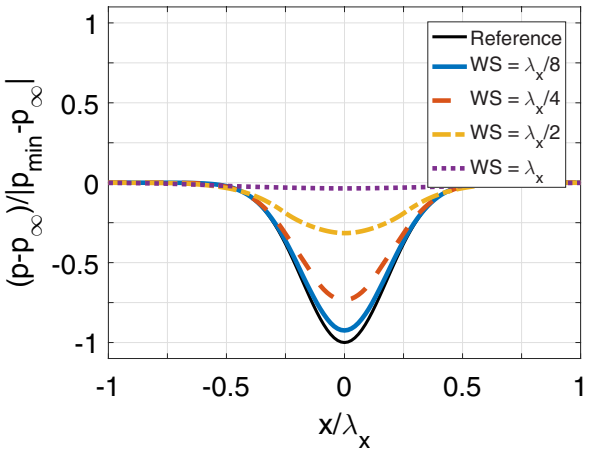

Figure 11. Pressure at $y = 0$ for different spatial resolutions.

To better show the impact of the temporal track length, figure 8 shows the peak response for the acceleration and pressure. For $\Delta T < 0.4\lambda_t$ the depicted peak response is rather similar to the transfer function from a Lagrangian perspective (see section 2.1). The figure shows a cut-off track-length of $\Delta T = 0.2\lambda_t$, based on a threshold of -3 dB. The -3 dB threshold is used here as reference point since it conveniently indicates the frequency at which the power of a filtered signal has dropped to 50% of its nominal passband value. Because the power of a signal is proportionate to the square of its amplitude, a 0.5 modulation of power level corresponds to a $0.5^{1/2} \approx 0.7$ modulation in amplitude.

The theoretically derived modulation presented here is consistent with the findings from de Kat and van Oudheusden (2012), who suggested to use a time separation so that $\Delta T < 0.1\lambda_t$. Based on a threshold of -3 dB however, their results suggested a cut-off time of $\Delta T = 0.2\lambda_t$. Figure 8 shows increasing deviations between the peak responses for acceleration and for pressure for track lengths above $\Delta T > 0.3\lambda_t$, for which multiple extrema exist (compare figure 6). The wavelength response (change in length scale) is not shown as the length scale for pressure does not vary for $\Delta T < 0.3\lambda_t$.

2.3. *Impact of spatial resolution*

To investigate the impact of the finite spatial resolution of the PIV measurement, the velocity input data are filtered before applying the pseudo-tracking approach. The spatial filtering associated with PIV depends on the specific implementation of the PIV processing as well as the properties of the velocity field (Schrijer and Scarano 2008, Theunissen 2012). The moving average filter is a widely accepted simplification and is also used here. The filter is implemented by first seeding a velocity field with a large number of imaginary particles and subsequently taking the average velocity of all particles within circular interrogation windows. The procedure is defined so that the interrogation window overlap is 50% and the central grid point is located at the vortex centre. Note that de Kat and van Oudheusden (2012) found little improvement for higher overlap factors.

Figure 9 shows the velocity along the line $y = 0$ for different spatial resolutions. Figures 10 and 11 show the corresponding acceleration and pressure profiles, respectively. Solid lines show the result after filtering. The figures show that the peak response decreases with increasing window size. Dotted lines depict analytically derived results, obtained according to $u_{\theta,\mathrm{piv}} = u_\theta \times T_{\mathrm{piv}}$ (figure 9) and

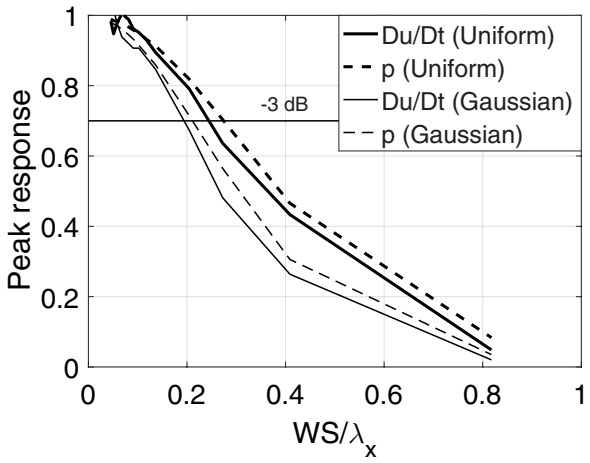

Figure 12. Peak response for material acceleration (Du/Dt) and pressure (p) as function of window size.

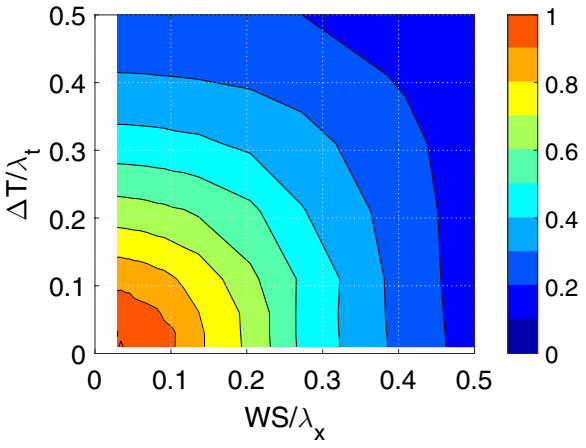

Figure 13. Peak response of pressure reconstruction as a function of flow time and length scales.

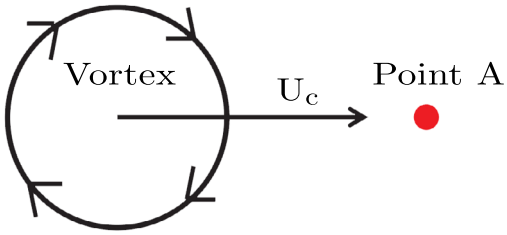

Figure 14. Schematic of vortex with point A.

$(Du/Dt)_{r,\mathrm{piv}} = (u_\theta T_{\mathrm{piv}})^2/r = (Du/Dt)_r\, T_{\mathrm{piv}}^2$ (figure 10), where $T_{\mathrm{piv}} = \mathrm{sinc}(\mathrm{WS}/\lambda_x)$ is the transfer function of a moving average filter used here as a approximate formulation of the spatial filtering by PIV. The transfer function for actual PIV processing may deviate from this approximation (Schrijer and Scarano 2008, Theunissen 2012). Comparison between the solid and dotted lines shows that the profiles obtained by pseudo-tracking applied to a spatially filtered velocity field can be accurately reproduced by means of transfer functions for window sizes $\mathrm{WS} < \lambda_x/4$.

To further quantify the dependence on window size, figure 12 shows the peak response for the material acceleration and pressure as a function of spatial resolution. In addition to the results obtained with top-hat weighted circular interrogation windows for which all particles within the interrogation window are treated similarly, the figures also include the results obtained by applying Gaussian weighting to interrogation windows with twice the nominal window radius (LaVision 2015). Figure 12 indicates a cut-off window size of $\mathrm{WS} \approx 0.2{-}0.3\lambda_x$, based on a threshold of -3 dB, depending on the weighting function used.

These findings are consistent with de Kat and van Oudheusden (2012), who suggested to use a spatial resolution so that $\mathrm{WS} < 0.05\lambda_x$ (accounting for the different definition of length scale). Based on a threshold of -3 dB, their results however also showed a cut-off wavelength of $\mathrm{WS} \approx 0.2\lambda_x$.

2.4. Combined impact of temporal and spatial resolution

To show the combined impact of temporal and spatial resolution, figure 13 shows the peak response as function of flow time and length scales. The depicted results have been obtained using a Gaussian weighting function (see discussion above). The figure shows that in order to limit the peak-response to a minimum of 0.7 (corresponding to -3 dB reduction), the track length and spatial resolution should satisfy

$$\left(\frac{\mathrm{WS}}{\lambda_x}\right)^2 + \left(\frac{\Delta T}{\lambda_t}\right)^2 < 0.2^2. \tag{5}$$

2.5. Impact on frequency pressure spectrum

Unsteady flow behaviour is often characterised and analysed by considering the energy spectra of (surface) pressure data. So far, we considered the case of a stationary vortex with a constant size and strength, so that the pressure evaluated at a particular location is constant. In general, the fluid pressure can vary in time because of

(i) Movement of structures, i.e. convection with the flow;
(ii) Changes in the size and shape the structure over time, e.g. due to diffusion or interaction with neighbouring vortices;
(iii) Acoustic waves that originate from nearby flow phenomena.

Pressure fields reconstructed from velocity data may exhibit additional temporal variations because of

(iv) Random errors in the input velocity fields;
(v) Non-constant boundary conditions used for the spatial integration of the pressure gradient.

The present section considers the impact of pseudo-tracking on the energy spectrum of a pressure signal obtained at a fixed point A in space while a vortical structure passes by at a constant velocity (U_c) (see figure 14). For the purpose of the analysis, the vortex does not interact with other structures and does not change significantly in terms of size and strength. Further it is assumed that the velocity input data are free of random errors.

As the vortex passes, point A will see the pressure distribution along the vortex symmetry line. The distance between

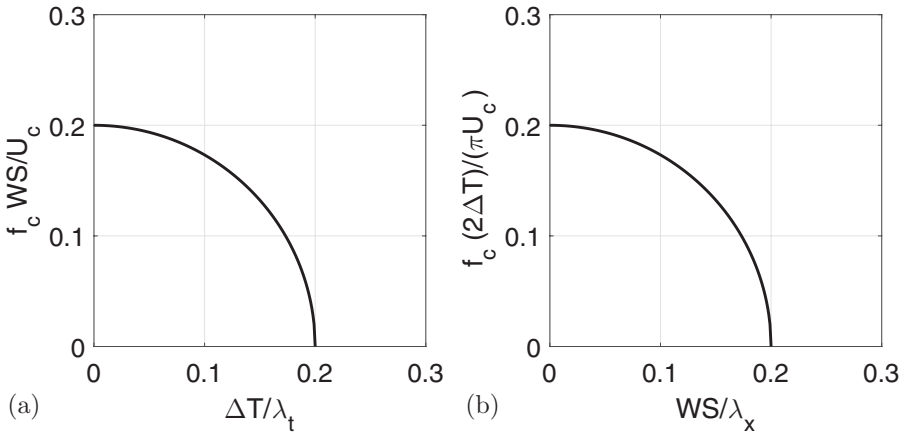

Figure 15. Cut-off frequency for the convection of flow structures as function of (a) flow time scale and (b) flow length scale.

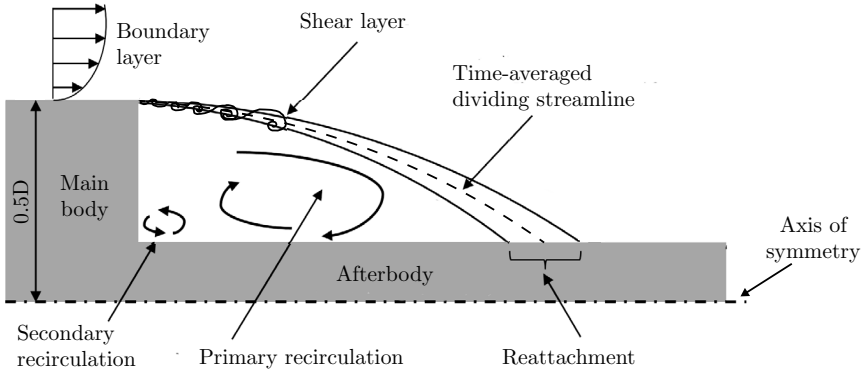

Figure 16. Schematic of mean flow topology.

point A and the vortex core is proportional to the time $t \propto U_c/r$. The pressure evaluated at point A, expressed as a function of time, represents a signal with an amplitude $A = p_{\text{peak}}\text{PR}$ and a frequency $f = U_c/\lambda_x$, where p_{peak} represents the minimum or maximum true pressure associated with a structure and PR represent the amplitude (peak-response) modulation due to spatio-temporal filtering (see section 2.4). Using equation (5), the cut-off frequency can be defined as

$$f_c = \frac{U_c}{\text{WS}}\sqrt{0.2^2 - \left(\frac{\Delta T}{\lambda_t}\right)^2} \tag{6}$$

or as

$$f_c = \frac{U_c}{V_{\theta,\max}}\frac{\pi}{2\Delta T}\sqrt{0.2^2 - \left(\frac{\text{WS}}{\lambda_x}\right)^2}. \tag{7}$$

Figure 15 illustrates the dependence of the cut-off frequency on the flow time scale and length scale, e.g. flow structures with time scale $\Delta T = 0.1\lambda_t$ can contribute to the energy content in the frequency band $f_c\,\text{WS}/U_c = 0{-}0.17$. The specific frequency to which an individual flow structure with time scale $\Delta T = 0.1\lambda_t$ contributes, depends on its length scale λ_x. The figures show that no meaningful contributions to the energy content can be expected for frequencies above $f_c = 0.2U_c/\text{WS}$ (figure 15(a)) or $f_c = (U_c/V_{\theta,\max})(\pi/10\Delta T)$ (figure 15(b)). Furthermore, the frequency band to which structures can contribute decreases for larger time scales and length scales and no contribution can be expected from structures for which $\Delta T > 0.2\lambda_t$ (figure 15(a)) or $\text{WS} > 0.2\lambda_x$ (figure 15(b)).

3. Experimental arrangements

Following the theoretical analysis framework presented in the previous section, the performance of pseudo-tracking is further characterised in an experimental assessment, with a specific focus on spatio-temporal filtering.

3.1. Description of the flow case

The assessment considers an axisymmetric base flow at a freestream velocity of 10 m s^{-1} for which the flow conditions allow time-resolved PIV measurements to be obtained (see introduction for more detail on the choice of flow case). Figure 16 provides a schematic representation of the mean flow organisation, viewed from the side. A three-dimensional representation of the geometry is provided by figure 17.

Due to the abrupt change in geometry, the flow separates at the trailing edge of the main body. A recirculation region is formed that is separated from the outer flow by a shear layer, which impinges downstream on the afterbody. Instantaneously, in the upstream part of the shear layer close to the base, Kelvin–Helmholz instabilities give rise to the development of vortical structures. Here, the shear layer behaves like a mixing layer between the high-momentum fluid in the outer flow and the

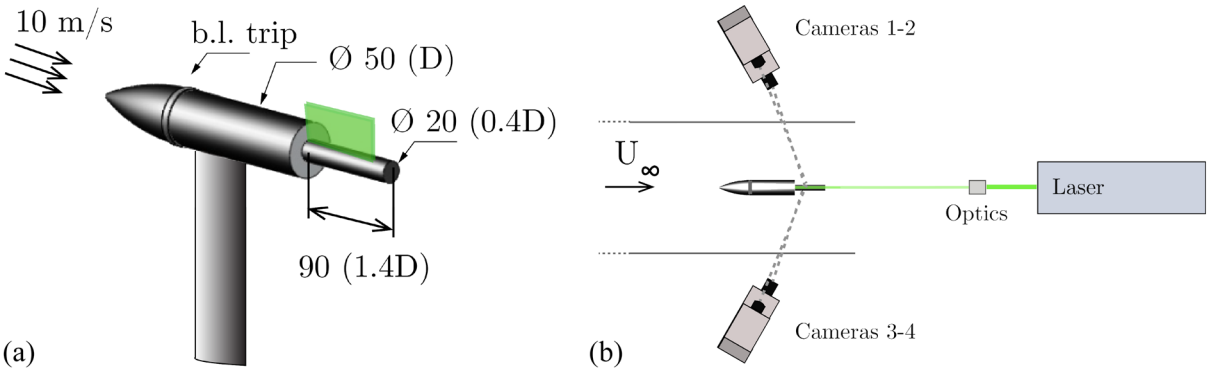

Figure 17. Sketches of (a) model geometry, adapted from Gentile *et al* (2016) and (b) PIV setup. The semi-transparent green region in the left figure indicates the PIV measurement volume.

low-momentum fluid in the recirculation region. Vortical structures may escape the shear layer (vortex shedding), while other structures may follow the shear layer and break down towards reattachment. This leads to a plethora of smaller, interacting structures, which may either convect downstream or be fed into the recirculation bubble, where they may eventually interact with a next generation of structures formed in the shear layer.

3.2. Flow facility and model

The measurements are conducted in the low-speed wind tunnel (W-Tunnel) of the Aerodynamics Laboratories of Delft University of Technology. The freestream velocity (U_∞) of the flow is 10 m s^{-1} and the Reynolds number based on the model diameter (Re_D) is about 35 000. The model is an ogive-cylinder with a diameter (D) of 50 mm equipped with an afterbody (see figure 17). The afterbody has a diameter of 20 mm (0.4D) and a length of 90 mm (1.8D). The model is supported by a thin wing-shaped airfoil (NACA 0018, 60 mm chord length). Transition of the incoming boundary layer is forced on the upstream part of the model by randomly distributed carborundum particles with a mean diameter of 0.8 mm on an 8 mm wide strip (Gentile *et al* 2016). The afterbody contains pinholes for the measurement of pressure fluctuations via microphones. The spacing between neighbouring pinholes is 10 mm (0.2D). The pinholes have a diameter of 1.0 mm and a length of 2.0 mm, resulting in an orifice aspect ratio of 2, which is equal to the threshold suggested by Shaw (1960). Mean pressure measurements are obtained at the same streamwise locations using a different afterbody model with 0.5 mm-diameter pinholes.

3.3. Reference pressure measurements

Omnidirectional back electret condenser microphones of the type Panasonic WM61A (6 mm diameter, nominal sensitivity of -35 ± 4 dB at 1 kHz equivalent to 18 mV Pa^{-1}) are mounted behind the pinholes in the afterbody. The space behind each microphone is filled with plasticide to ensure an airtight sealing. For measurements concurrent with PIV, three microphones are mounted simultaneously. For measurements without PIV, the same microphone is mounted successively in different pinholes to reduce the impact of differences in microphone characteristics. The microphones are connected to custom-made 3V battery-powered preamplifiers that incorporated a low-pass filter with a cut-off frequency of about 3 kHz. The preamplifiers are connected to a 16-bit National Instruments (NI) 9215 data acquisition system installed in a NI cDAQ-9172 chassis. The system also records the trigger signal of the PIV-measurements to enable synchronisation. All connections are made using shielded coaxial cables to avoid any crosstalk. Sampling is performed at 50 kHz per microphone.

Inspired by Wong (2014), the gain and phase shift of each microphone-pinhole-amplifier combination as a function of frequency is obtained by calibration against a reference microphone (see appendix for details of the calibration procedure). The frequency response is used to correct the measured signals by means of deconvolution. The transfer function of the system in terms of phase shift and gain depends on the microphone, the pinhole and the mounting of the microphone in the pinhole. Each microphone-pinhole-amplifier combination is therefore calibrated individually.

Figure 18 shows the phase shift and gain within the frequency range of interest for the same microphone placed in different pinholes. The general trend of the lines shows that the gain and phase shift are relatively constant over the depicted range with typical values of 60 ± 10 mV Pa^{-1} and $-10 \pm 10°$, respectively. A reduction in gain and increase in phase shift can be observed towards the lower end of the frequency range, which is a typical feature of microphones (Wong 2014). In addition, the spectral noise can be seen to increase for lower frequencies, which is attributed to poor statistical convergence and difficulties generating such signals with non-specialised equipment. No reliable calibration could therefore be obtained for frequencies below approximately 20 Hz, which is defined as the lower measurement threshold indicted by the red vertical line in figure 18. This frequency corresponds to a value of the Strouhal number based on the model diameter ($\mathrm{St}_D = fD/U_\infty$), of $\mathrm{St}_D = 0.1$.

All microphone measurements were validated by checking their power spectral densities for any anomalies. It was confirmed that the background noise was at least an order of

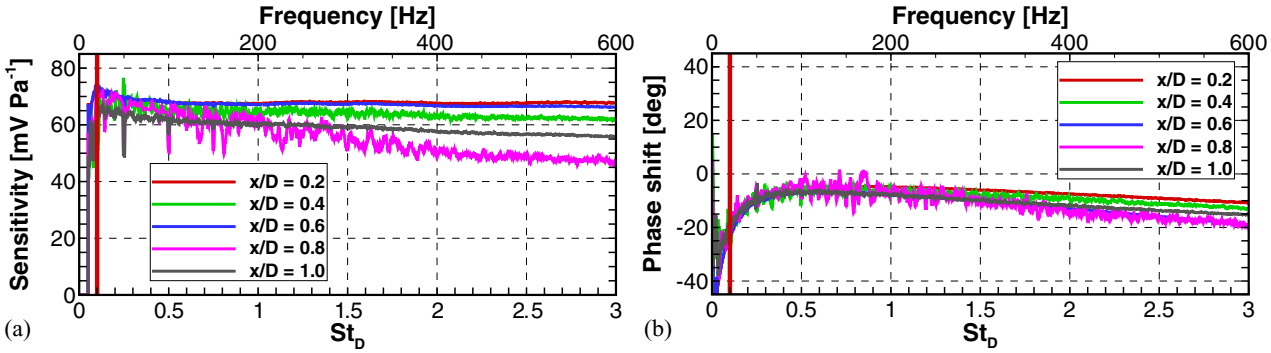

Figure 18. Frequency response of measurement microphone placed in different pinholes. The vertical red line indicates the lower frequency for which the calibration is deemed reliable.

magnitude lower than the measured flow-related pressure fluctuations.

3.4. PIV measurements

Tomographic PIV measurements were performed in a relatively thin volume that was located downstream of the step and over the afterbody surface, covering the region where the pressure transducers are located (see figure 17(a)). The size of the measurement volume is $1.5D \times 0.7D \times 0.07D$ (75 mm × 35 mm × 3.5 mm, $L \times H \times W$).

The flow is uniformly seeded by a SAFEX smoke generator with tracers of 1 μm. The typical seeding concentration is 0.05 particles per pixel (ppp). Illumination is provided by a Quantronix Darwin Duo Nd-YLF laser (2 × 25 mJ/pulse at 1 kHz). The laser beam is directed onto the model base after being shaped to into a light sheet with a thickness of about 4 mm.

Particle images are recorded by four Photron FastCAM SA1.1 CMOS cameras (maximum resolution 1024 × 1024 pixels, 20 μm pixel pitch) placed at opposite sides of the test section. All cameras are placed at a yaw angle of about 30° to receive forward scattered light. Two cameras, equipped with 60 mm Nikon objectives, are located at the same height as the base of the model at either side of the field of view. The two other cameras are placed to view from above at a pitch angle of about 40°. These cameras are equipped with 105 mm Nikon objectives. The objectives are installed on a tilt mechanism to satisfy the Scheimpflug condition. Their aperture is set to *f*/5.6. The magnification is 0.23 and the resulting digital resolution is 12.3 pixel mm^{-1}.

Images of 1024 × 512 pixels are recorded at 10 kHz in single-frame mode, leading to a time separation of 100 μs, corresponding to a freestream particle displacement of 12 pixels. Each recording consists of 10 941 images over a time span of about 1.1 s.

The particle images are enhanced by subtracting the local minimum intensity over a 101 × 101 pixel kernel and by subtracting the minimum intensity within 31 × 31 pixel kernels. The resulting intensity is normalised by a min–max filter with a kernel size of 6 × 6 pixels. Gaussian smoothing (Thomas *et al* 2010) and sharpening is applied to obtain better defined particles. This approach was empirically found to reduce the number of outliers in the velocity fields obtained after further processing. The resulting particle image size is about 2.5 pixels, leading to a source density (N_s) of about 0.25.

After volume self-calibration (Wieneke 2008), reconstructed volumes are obtained by 25 iterations of the SMART algorithm after initialisation by the MLOS algorithm. Voxels with intensities below 0.01 counts are not updated (Atkinson and Soria 2009). Gaussian smoothing is applied after each iteration (Discetti *et al* 2013), excluding the final iteration. The resulting reconstructions have a signal-to-noise ratio (SNR) of about 5.

Cross-correlation of the reconstructed objects is performed using iterative multi-grid volume deformation (based on Scarano and Riethmuller (2000)), symmetric block direct correlation (Discetti and Astarita 2012) and Gaussian window weighting of the intensity in spherical interogation volumes. After each correlation step, spurious vectors are identified by universal outlier detection (Westerweel and Scarano 2005) and replaced using linear interpolation. Intermediate vector fields are filtered before the next iteration by Gaussian smoothing. For the final three iterations the nominal interrogation volumes size is set at 16 voxels (leading to Gaussian weighting of spherical volumes with a diameter of 32 voxels, LaVision (2015)). Each final (nominal) window contains about 7 particles. The overlap of the volumes is 75%, resulting in a vector spacing of 0.33 mm (4 voxels).

A masking procedure was applied throughout the processing to reduce the impact of reflections of the laser light of the model and to only obtain velocity values in the regions where particle images of are deemed to be of sufficient quality. First, in the particle images, pixels are disabled that show parts of the model or laser light reflections, identified by visual inspection. Next, during tomographic reconstruction, only those regions are reconstructed for which at least three out of four particle images contain valid pixels. Finally, during the cross-correlation of tomographic volumes, vectors are only obtained for correlation windows with at least 50% valid voxels.

3.5. Calculation of material acceleration and pressure

Material acceleration fields are calculated from the PIV velocity fields according to the procedure described in van

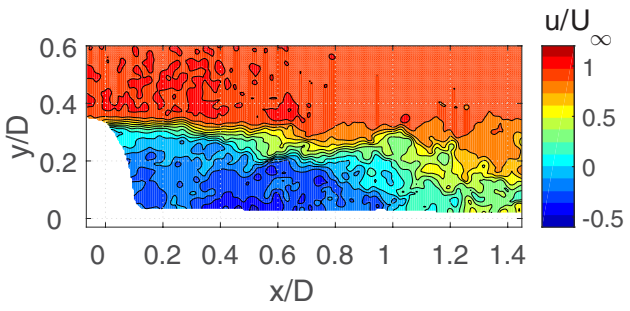

Figure 19. Representative example of instantaneous streamwise velocity.

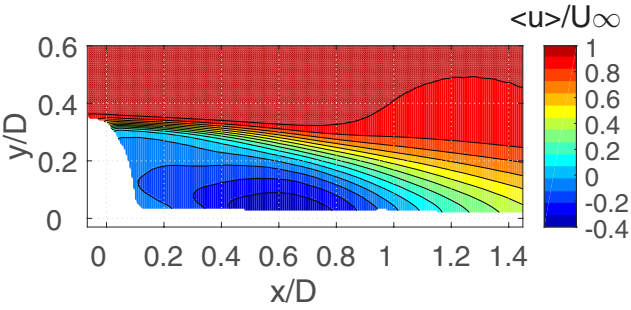

Figure 20. Mean streamwise velocity.

Gent *et al* (2018); section 2. Six integration/interpolation steps are carried out between subsequent PIV velocity fields, ensuring that the CFL condition is met throughout the domain. The material acceleration is calculated using first-order least-square fitting (LS).

Pressure fields have been calculated by solving the momentum equation for pressure. Motivated by the high Reynolds number of the flow, the contribution of the viscous term is neglected. The problem is discretized using a similar discretisation as Jeon *et al* (2015) and the resulting system of linear equations is solved via the use of QR decomposition. Neumann boundary conditions are implicitly imposed on all sides except for the top surface of the domain. There, the mean static pressure as obtained from Bernoullis equation is prescribed as a Dirichlet boundary condition:

$$p_t = p_\infty + \frac{1}{2}\rho U_\infty^2 = p_{\mathrm{BC}} + \frac{1}{2}\rho \bar{V}_{\mathrm{piv}}^2. \tag{8}$$

Here, p_t is the total pressure measured by a pitot-static tube, p_{BC} is the pressure used as boundary condition and $\bar{V}_{\mathrm{piv}}$ is the mean velocity obtained from PIV. The use of mean pressure values instead of instantaneous pressure values is motivated by observations that strongly suggested that fluctuations in freestream pressure levels calculated via Bernoullis equation primarily originate from velocity measurement noise, rather than physical velocity fluctuations. Pressure is normalised by subtracting freestream static pressure and dividing by freestream dynamic pressure: $C_p = (p - p_\infty)/\frac{1}{2}\rho U_\infty^2$.

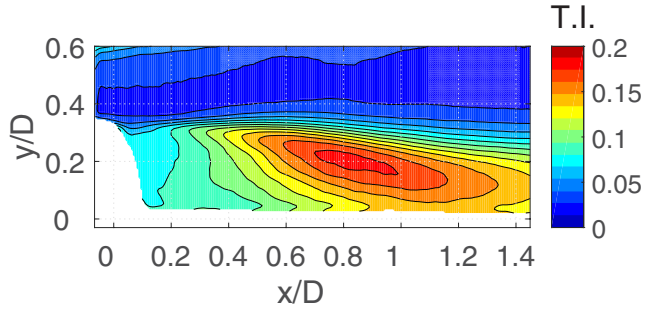

Figure 21. Turbulence intensity.

The use of longer tracks in the pseudo-tracking approach reduces the impact of random PIV measurement errors but may filter out relevant flow scales. To assess the impact of track length, the procedure is implemented by calculating tracks with nominal lengths of 5, 15 and 25 velocity fields ($N_{\mathrm{piv}} = 5$, 15 and 25; being equivalent to $n_{\mathrm{piv}} = 2$, 7 and 12). Due to truncation of tracks at the boundaries of the domain, locally the effective track length is shorter. The impact of truncation becomes greater for longer nominal tracks as progressively more tracks are truncated. For the aforementioned nominal track lengths, the average effective track length (N_{eff}) is about 4, 13 and 18.

4. Experimental results

4.1. Velocity results

To characterise the velocity measurements and the flow field, figures 19 and 20 depict a realisation of the instantaneous streamwise velocity field and the mean streamwise velocity, respectively. The mean velocity has been obtained using a time-resolved sequence of 21 800 velocity fields covering a duration of 2.18 s. The mean flow field shows that mean reattachment of the shear layer occurs at approximately $x/D = 1.0$. Below the shear layer, in the separated region the mean velocity reaches a minimum of about $-0.37U_\infty$.

Figure 21 shows the normalised turbulence intensity (T.I.) which is defined as

$$\mathrm{T.I.} = \sqrt{\frac{\sigma_u^2 + \sigma_v^2 + \sigma_w^2}{3U_\infty^2}} \tag{9}$$

where σ_u^2, σ_v^2 and σ_w^2 denote the variances of the velocity components in x-, y- and z-direction, respectively.

Highest levels of turbulence intensity can be observed in the downstream part of the shear layer and the reattachment region, with a maximum of $\mathrm{T.I.}_{\max} = 0.20$ at about $x/D = 0.73$; $y/D = 0.24$. The turbulence intensity in the shear layer in the direct vicinity of the step is relatively low. This is attributed to the limited spatial resolution of the experimental data, which prevents the flow dynamics to be properly sampled in this region. Further, the turbulence intensity decreases towards

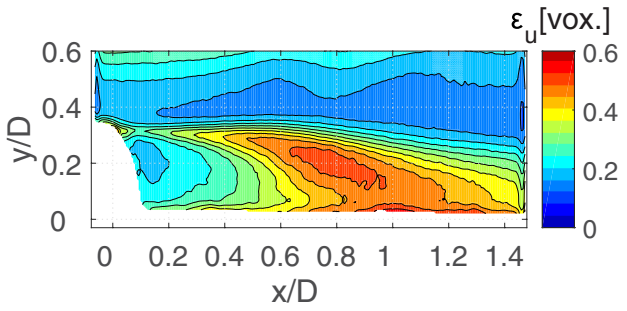

Figure 22. Random error estimate aggregated over all z-planes.

reattachment, which may be attributed to (1) a decrease in characteristic flow length scales due to break down of vortices and the associated increased impact of spatial filtering in the correlation analysis, (2) increase in the shear layer thickness, and (3) oscillations in the reattachment length. The latter two aspects of the flow cause the turbulent energy that is present in the shear layer to be spread over a wider area in a statistical sense.

In absence of any reference velocity value, error estimates of the resulting velocity fields can be obtained by considering that in an incompressible flow, any nonzero value of the velocity divergence can be ascribed to measurement errors (Scarano and Poelma 2009, Lynch and Scarano 2014a). An error estimate is defined as the difference between the measured values and solenoidal filtered measurements, obtained via solenoidal waveform reconstruction (SWR, see Schiavazzi *et al* (2014)). The mean difference is taken as estimate for the bias error and the standard deviation of the difference is taken as estimate for the random error. The random error estimate is plotted in figure 22. Quantities are expressed in voxels displacement, where 1 voxel displacement corresponds to $0.1U_\infty$. Error estimates have been aggregated over all z-planes. The error components for the other individual components look similar, with the error of the w-component being about 0.05 voxel higher. It is noted that a comparison to solenoidal filtered results underestimates the true error by implicitly assuming that the errors in velocity measurements in neighbouring grid points are uncorrelated, which is not the case. Lynch and Scarano (2014a), who applied the same principle to a similar flow case with similar experimental arrangements quantified an underestimation of about 30%. Even so, the error estimates obtained here are deemed suitable to provide an indication of the distribution and magnitude of the errors in the PIV velocity fields.

Figure 22 shows that the random error is estimated to be smaller than 0.50 voxel displacement. Relatively low error estimates are observed in the freestream, where the error estimate typically is below 0.15 voxel displacement. Elevated levels are observed near the top of the measurement domain which are attributed to poor illumination conditions. The largest error estimates are found in the separated shear layer and the reattachment region where the largest displacement gradients and smallest spatial and temporal scales occur. In general, the error estimates for the present experiment are within the typical range of uncertainties of tomographic PIV reported for similar flows and experimental arrangements (Lynch and Scarano 2014a, 2014b, van Gent *et al* 2017). Bias errors (not shown for brevity) are estimated to be lower than 0.02 voxel displacement, except in a small region in the shear layer in the direct vicinity of the step, where the maximum bias error estimate attains a maximum value of 0.10 voxel displacement.

4.2. Instantaneous material acceleration and pressure

Figure 23 shows a representative example of the instantaneous material accelerations in streamwise direction (left figures) and reconstructed pressure fields (right figures). From top to bottom the figures have been calculated on the basis of nominal track lengths of 5, 15 and 25 PIV velocity fields. The material acceleration fields shows small-scale flow structures in the shear layer and reattachment region. No structures are visible in the shear layer directly downstream of the step, which is attributed to limitations in spatial resolution (similarly as for the turbulence intensity).

Comparison of the results shows that for longer tracks, fewer structures can be observed and the observed structures have lower extreme values (i.e. lower maxima or higher minima). This is in line with the theory from section 2, according to which longer tracks result in increasing amplitude modulation that is more pronounced for smaller structures. The length scales of reconstructed structures and their dependence on the track length are further investigated in section 4.4.

Figure 24 shows a representative sample of the PIV pressure and microphone pressure at $x/D = 0.6$ to illustrate the relative agreement between both signals. The PIV pressure has been calculated using tracks over 15 velocity fields ($N_{\mathrm{piv}} = 15$). The figure represents data of 3240 PIV snapshots and 15 000 microphone measurements. Both signals have been low-pass filtered with a cut-off frequency of $\mathrm{St}_D = 0.8$ (160 Hz). The figure already indicates a good qualitative agreement between the PIV pressure signal and microphone signal, which is further investigated in the following sections.

4.3. Mean pressure and pressure fluctuations

Figures 25 and 26 show the mean PIV-based pressure and the RMS of pressure fluctuations, respectively. The depicted statistical quantities have been obtained using a time-resolved sequence of 21 800 pressure fields covering a duration of 2.18 s. Pressure fields have been calculated using a nominal track length of 25 velocity fields ($N_{\mathrm{piv}} = 25$), as the PIV pressure spectra for that track length showed the best agreement with the microphone pressure spectra (see section 4.5).

The mean pressure field (figure 25) shows a low-pressure region in the upstream part of the measurement volume where a minimum of $C_{p,\mathrm{min}} = -0.26$ is attained at $x/D = 0.6$; $y/D = 0.2$ In the downstream part of the measurement volume a high-pressure region occurs, where a maximum mean pressure $C_{p,\mathrm{max}} = 0.10$ is attained at $x/D = 1.2$. Consistent with literature, the maximum pressure occurs downstream of the point of mean reattachment ($x/D = 1.0$) (e.g. Deck and Thorigny (2007)).

The highest levels of pressure fluctuations (figure 26) can be observed to occur in the downstream part of the shear layer, with a maximum of $C'_{p,\mathrm{RMS,max}} = 0.08$ located at $x/D = 0.75$;

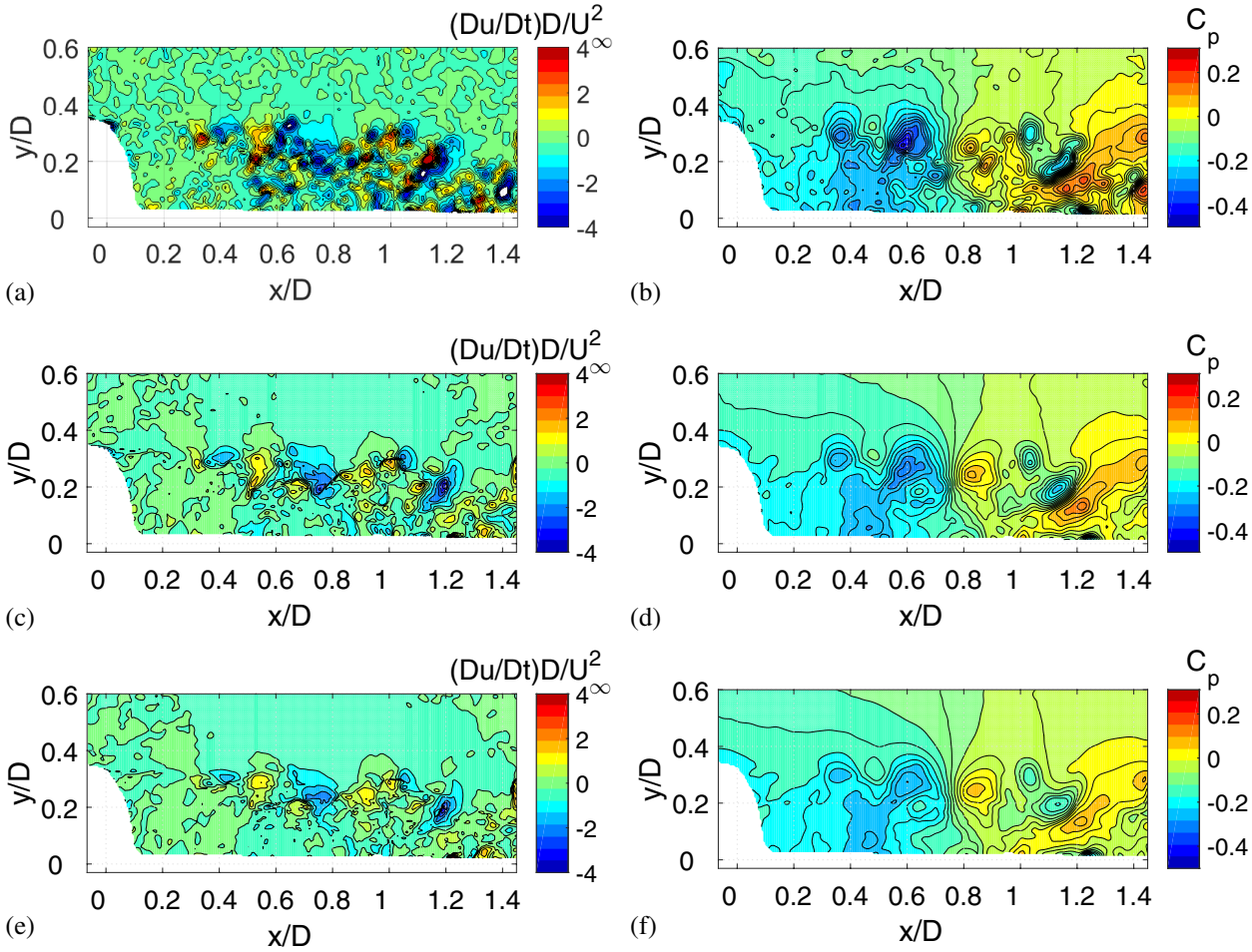

Figure 23. Representative examples of instantaneous material acceleration in streamwise direction (left) and corresponding pressure in the centre-plane (right) calculated based on 5, 15 and 25 PIV velocity fields (top to bottom).

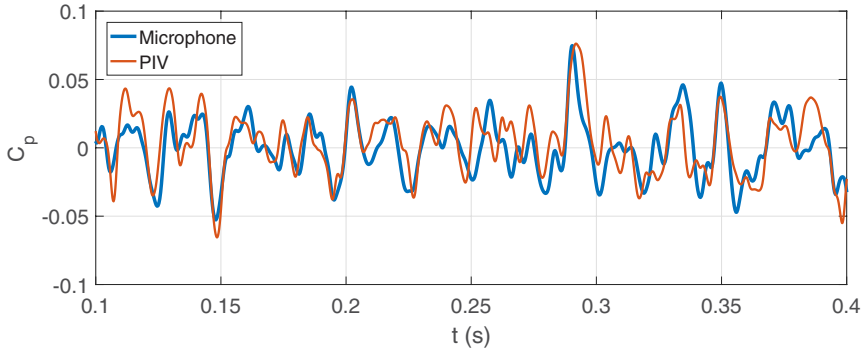

Figure 24. Representative samples of the microphone and PIV pressure signal, low-pass filtered with a cut-off frequency $St_D = 0.8$.

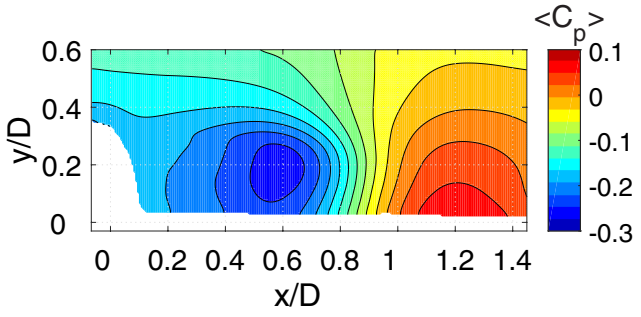

Figure 25. Mean pressure.

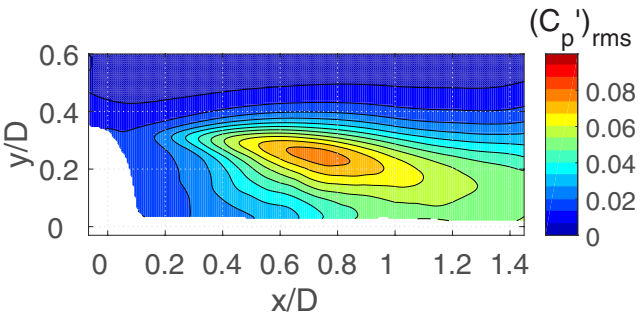

Figure 26. RMS of pressure fluctuations.

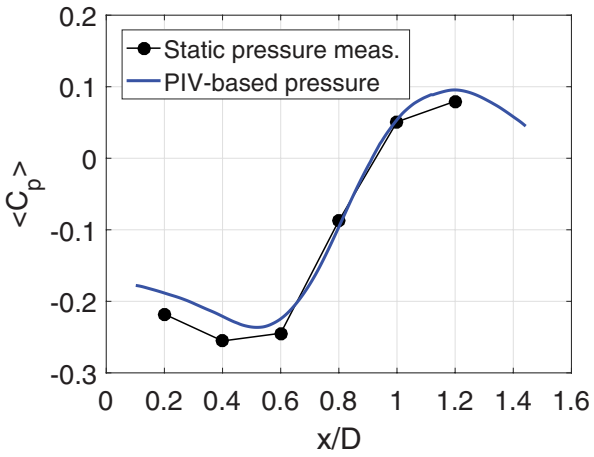

Figure 27. Mean pressure on the afterbody.

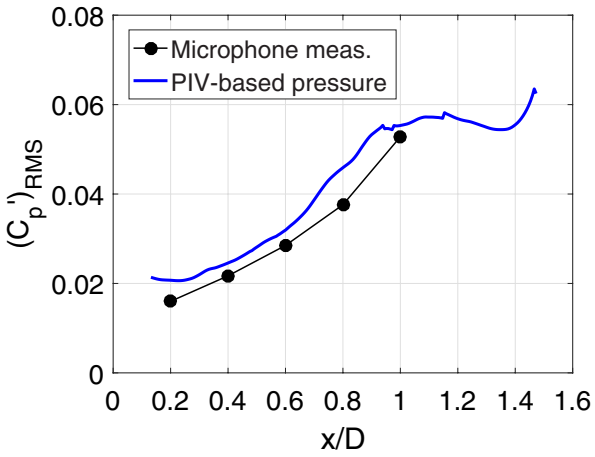

Figure 28. RMS of pressure fluctuations on the afterbody.

$y/D = 0.24$. As for the turbulence intensity (figure 21), the pressure fluctuation levels are relatively low in the vicinity of the step and decrease towards reattachment.

To validate the PIV-based pressure, figures 27 and 28 compare the PIV-based pressure along the centreline across the bottom of the PIV measurement domain, to the direct surface pressure measurements at the afterbody. The mean PIV-based pressure (figure 27) shows a good agreement with the sensor measurements with a maximum discrepancy (ΔC_p) of 0.03. For streamwise positions $x/D < 0.5$ and $x/D > 1.0$, the PIV-based pressure is slightly higher, which may be the result from the small distance between the PIV pressure domain and the afterbody surface.

Figure 28 shows a reasonably good agreement of the PIV results with the microphone measurements, both in terms of level and trend. The fluctuation levels are about 0.005 higher for the PIV results, which represent about 15% of the average fluctuation levels as determined by the microphones. This difference can at least partly be attributed to the small distance between the PIV pressure domain and the afterbody as well as the high-pass filtering as part of the microphone calibration procedure (see section 3.3). A spectral analysis (see section 4.5) revealed that the higher levels for PIV are not due to higher noise levels in the PIV-based pressure (at least not for track lengths over 25 velocity fields, $N_{\mathrm{piv}} = 25$). A maximum fluctuation level occurs just upstream of the mean reattachment point which is consistent with other results found in literature (e.g. Deck and Thorigny (2007)). The increase in PIV-based pressure at $x/D > 1.4$ is attributed to the impact of truncation of tracks in the corner of the domain, resulting in shorter tracks and higher noise levels.

4.4. Characterisation of length scales

To further characterise the length scales present in the reconstructed pressure fields, figure 29 shows the wavenumber spectra of velocity and pressure fluctuations along the line $y/D = -0.11$ up to the maximum measureable wavelength $\lambda_x = \mathrm{WS}/2$ according to the Nyquist–Shannon sampling theorem. The spectra are obtained using the fast Fourier transform of the detrended signal obtained by subtracting the straight line that passes through the first and last samples in the signal). No windowing function was used (Foucaut *et al* 2004, Liu and Katz 2013). The spectra from 1000 snapshots were averaged to obtain a converged result.

The velocity and pressure spectra can be seen to follow a $-5/3$ and $-7/3$ power law, respectively, characteristic of isentropic turbulence (Pope 2000). Although it is recognized that the flow in the present domain is not isentropic, the agreement of the PIV-based spectra with theory satisfies the present need. For $\mathrm{WS}/\lambda_x > 0.45$, the velocity spectra start to deviate from the $-5/3$ power law. This behaviour is consistent with the expected filter behaviour of the correlation analysis, which is commonly modelled by: $T_{u,\mathrm{PIV}} = \mathrm{sinc}\,(\mathrm{WS}/\lambda_x)$. Foucaut *et al* (2004) define a cut-off wave number of $k_c = 2.8/\mathrm{WS}$, corresponding to $\mathrm{WS}/\lambda_c = 2.8/2\pi = 0.45$. To illustrate the behaviour of this filter, figure 29 includes the sinc-filtered isentropic turbulence spectrum as a simplified model for the PIV spectra (Foucaut *et al* 2004). Comparison between the model and the PIV spectra supports the assumption that the change in slope of the PIV-spectra for $\mathrm{WS}/\lambda_x > 0.45$ is indeed a result of spatial filtering. Deviations between the model and the PIV spectra for $\mathrm{WS}/\lambda_x > 0.60$ are attributed to spectral noise.

For the pressure spectrum, pseudo-tracking and pressure integration lead to additional filtering. At $\mathrm{WS}/\lambda_x = 0.2$, the pressure spectrum for $N_{\mathrm{piv}} = 5$ starts to deviate from the $-7/3$ power law, which is in perfect agreement with the cut-off window size found in section 2.3. Comparison of the spectra for longer track lengths shows that selecting a longer nominal track length reduces the energy content for all length scales, which is in agreement with the theory from section 2.4 (compare figure 13). These observations suggest that for $N_{\mathrm{piv}} = 5$, the amplitude modulation due to pseudo-tracking is predominantly defined by the spatial resolution of the PIV measurement, whereas for $N_{\mathrm{piv}} = 15$ and 25 the impact of temporal resolution (set by the track length) becomes substantial.

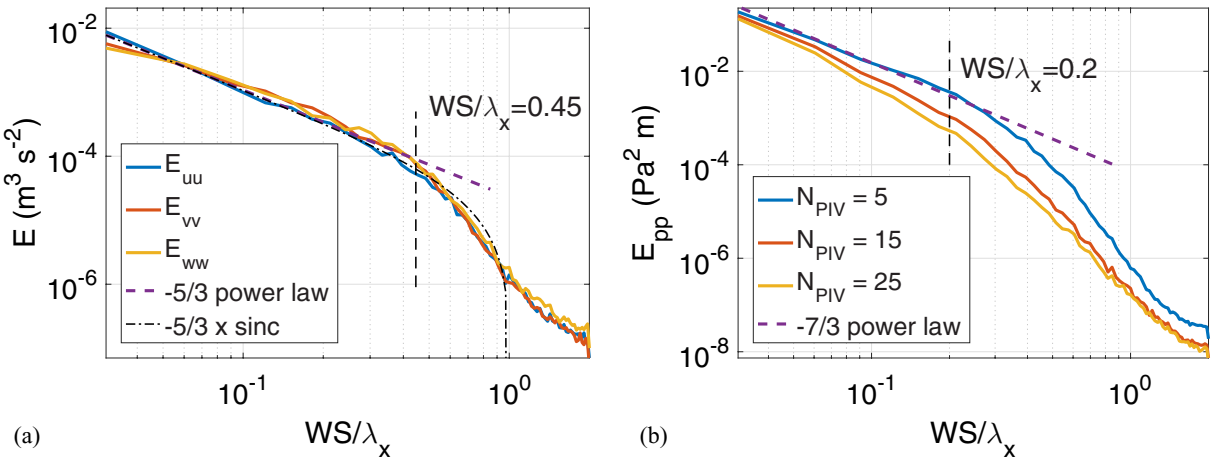

Figure 29. Wavenumber spectra along $y/D = 0.11$ for (a) velocity and (b) pressure.

4.5. Spectral analysis

Figure 30 shows the power spectral density of the microphone and PIV pressure signals for different streamwise locations and track lengths. The x-axis shows on a logarithmic scale the Strouhal number up to $\mathrm{St}_D = 15$ (3000 Hz) which corresponds to the cut-off frequency of the analogue low-pass filter in the pre-amplifier. The Nyquist frequency of the PIV spectra is $f_{\mathrm{Nyquist}} = (2\Delta t_{\mathrm{piv}}^{-1}) = 5$ kHz ($\mathrm{St}_D = 25$). The depicted spectra are obtained from 2-minute microphone signals and 2 second PIV pressure signals. As a compromise between accuracy and spectral resolution, the spectral estimates are obtained by averaging the spectral information of windowed signal segments of 0.05 s with a 50% overlap (containing 2500 microphone measurements and 500 PIV measurements) according to Welch's method, resulting in a spectral resolution of $\Delta\mathrm{St}_D = 0.06$ (12.5 Hz).

The microphone spectra show maxima in energy density at about $\mathrm{St}_D = 0.2$ (40 Hz). Note that microphone spectra for frequencies smaller than $\mathrm{St}_D = 0.1$ (20 Hz) are underestimated as a result of the microphone calibration procedure (see section 3.3). Comparison of microphone spectra in the different figures shows an increase in energy density for more downstream positions, which is consistent with an increase in overall fluctuation levels towards reattachment (see figure 28). Although the presentation of spectra in figure 30 does not allow identification of distinct peaks, the overall distribution of energy density is consistent with a number of other studies that find peaks centred at $\mathrm{St}_D \approx 0.1$ and ≈ 0.2 as well as a broadband peak centred at about $\mathrm{St}_D \approx 0.6$, which are related to flapping of the shear layer, vortex shedding and vortical structures in the reattachment region, respectively (see e.g. Weiss *et al* (2009)). The origin of the distinct peaks in the microphone signals at $\mathrm{St}_D = 4.7$ (940 Hz) is attributed to the operation (acoustic noise) of the tunnel.

All PIV spectra show similar trends as the microphone spectra for frequencies in the range $\mathrm{St}_D = 0.2{-}0.8$. Deviations for frequencies below $\mathrm{St}_D = 0.2$, are attributed to the microphone calibration procedure (see section 3.3). Above $\mathrm{St}_D \approx 0.8$, the energy content in the microphone signal drops off. Only the PIV spectra for $N_{\mathrm{piv}} = 25$ follows the microphone spectra. The PIV spectra for $N_{\mathrm{piv}} = 5$ and $N_{\mathrm{piv}} = 15$ remain relatively high, which is attributed to the noise in the PIV pressure resulting from the increased error calculation incurred by the shorter track lengths.

The plateau in the PIV spectra for $N_{\mathrm{piv}} = 5$ above $\mathrm{St}_D \approx 0.8$ suggests the existence of a broadband noise floor. In that case, $\mathrm{St}_D \approx 0.8$ represents the crossover frequency (f_{cross}) at which the signal-to-noise ratio is equal to one. For lower frequencies ($f < f_{\mathrm{cross}}$) the signal-to-noise ratio is larger than one and for higher frequencies the signal-to-noise ratio is lower than one ($f > f_{\mathrm{cross}}$). Comparison of the PIV spectra for different track lengths suggest that the broadband noise is low-pass filtered with a cut-off frequency that is dependent on the track length. The observed cut-off frequencies seem to be consistent with the cut-off frequency for pseudo-tracking as derived in section 2.1 $f_c \approx 0.2\Delta T^{-1}$, which corresponds to $\mathrm{St}_D = 5$, 1.4 and 0.8 for nominal track lengths $N_{\mathrm{piv}} = 5$, 15 and 25, respectively.

To further assess the agreement of PIV and microphone pressure for different time scales, figure 31 shows their coherence as well as the normalised cross-correlation coefficient as function of the cut-off frequency of a low-pass filter that was applied to both signals. Different colours indicate different locations and different linetypes indicate different nominal track lengths. Values are based on 1.09 s of data containing 10 900 PIV pressure fields and 54 500 microphone measurements. PIV pressure signals were supersampled to match the sampling frequency of the microphone signal. Raw microphone signals were used to be able to include frequencies below $\mathrm{St}_D = 0.1$ for which no microphone calibration is available.

Figure 31(a) shows that the coherence attains a maximum in the range $\mathrm{St}_D \approx 0.1$–0.4, then decreases to attain a secondary peak in the range $\mathrm{St}_D \approx 0.6{-}0.8$, and then quickly drops for higher frequencies. The coherence is virtually independent of the selected track length. Figure 31(b) shows correlation values with maxima in the range of $\rho_{\mathrm{max}} = 0.6$ to 0.8. Variations in correlation values between different microphones may originate from differences in local flow dynamics and differences related to the microphone measurements. The figure shows that up to the frequencies for which the maxima occur, the correlation is strongly dependent on the passband and almost independent of the nominal track length. For

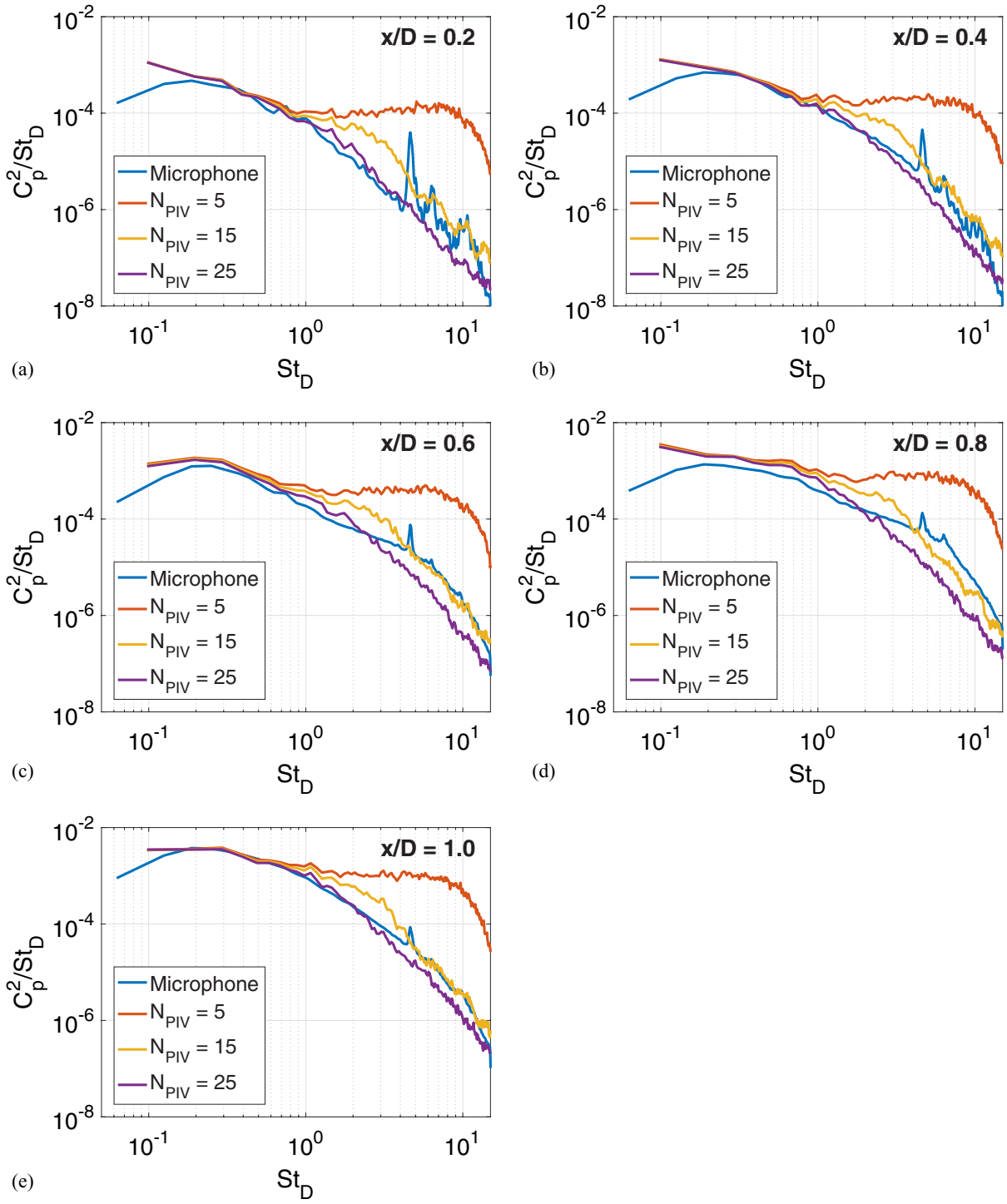

Figure 30. Estimated power spectral density of microphone and PIV pressure signals for (a) $x/D = 0.2$, (b) $x/D = 0.4$, (c) $x/D = 0.6$, (d) $x/D = 0.8$ and (e) $x/D = 1.0$.

higher frequencies, the correlation for $N_{\text{piv}} = 5$ rapidly deteriorates as a result of high frequency noise (compare figure 30). For longer track lengths, which have been observed to filter out most of the high frequency noise content, the decrease in correlation is less pronounced.

The relatively high coherence and correlation for all track lengths for frequencies below $\text{St}_D = 0.3$ indicate that the flapping of the shear layer and vortex shedding (e.g. Weiss *et al* (2009)) are reproduced regardless of the track length. The moderate coherence around $\text{St}_D \approx 0.6$ suggests that also flow phenomena associated with vortical structures in the reattachment region (e.g. Weiss *et al* (2009)) are partly captured. The drop in coherence and correlation for higher frequencies can be explained by the earlier observation from figure 30 that the pressure fluctuations in the flow drop below the noise floor or the measurement procedure.

With regards to the impact of spatial resolution, a cut-off frequency of $f_c = 0.2U_c/\text{WS}$ for the convection of flow

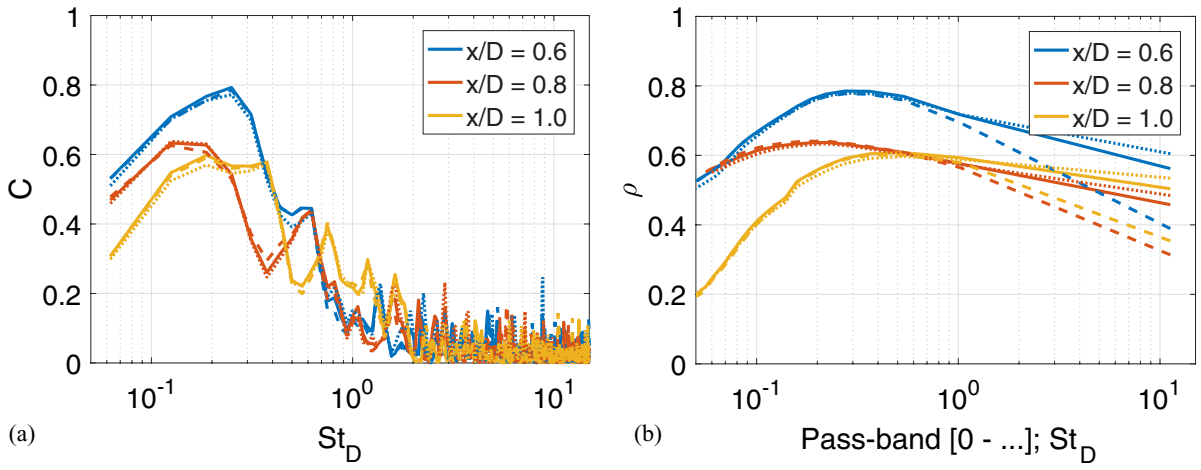

Figure 31. (a) Coherence and (b) correlation between PIV and microphone pressure; $N_{\text{piv}} = 5$ (dashed), $N_{\text{piv}} = 15$ (solid) and $N_{\text{piv}} = 25$ (dotted).

structures was derived in section 2.5. Based on the absolute velocity magnitude, the average convection velocity (U_c) of the flow over the afterbody is estimated to range from $U_c = 0.05U_\infty$ at $x/D = 1.0$ to $U_c = 0.35U_\infty$ at $x/D = 0.6$, which corresponds to cut-off frequencies in the range $\text{St}_D = 0.5{-}2.7$. Differences between PIV and microphone pressure results above $\text{St}_D = 0.5$ are therefore partly attributed to a lack of spatial resolution.

5. Determination of suitable track length and pressure noise level

The observations made in section 4.5 suggest that a suitable track length can be defined that filters out any energy content at frequencies higher than the crossover frequency. In practice, this track length may be identified and achieved using the following procedure:

(i) Apply pseudo-tracking with a short track length, e.g. $N_{\text{piv}} = 3$ or 5
(ii) Determine the crossover frequency from the resulting spectrum
(iii) Define a track length so that the cut-off frequency is similar to the crossover frequency: $f_c \approx 0.2\Delta T_{\text{optimal}}^{-1} \approx f_{\text{cross}}$.
(iv) Apply pseudo-tracking with the optimal track length, i.e. $N_{\text{piv}} = 2\Delta T_{\text{optimal}}/\Delta t_{\text{piv}}$

The level of the noise floor may be used to estimate the precision of the PIV pressure measurement. For instance, at $x/D = 0.2$, the noise level $(C_p^2/\text{St}_D)_{\text{noise}} \approx 10^{-4}$ (see figure 30(a)), from which it may be derived that the pressure measured at that location has an error margin of $\Delta C_p = \pm 10^{-2}$.

6. Conclusions

The spatio-temporal filtering behaviour of pseudo-tracking has been characterised using a theoretical/numerical assessment based on a generic two-dimensional Taylor vortex flow and an experimental assessment based on the flow over an axi-symmetric step.

The theoretical/numerical assessment showed how filtering along Lagrangian tracks leads to amplitude modulation of a vortex flow. It was found that in order to achieve a peak-response below 0.7 (corresponding to a 3 dB reduction in energy), the track length and spatial resolution should satisfy $(\text{WS}/\lambda_x)^2 + (\Delta T/\lambda_t)^2 < 0.2^2$. Here, WS is the size of the interrogation window used in the PIV analysis, $2\Delta T$ is the time covered by the (pseudo-)track and λ_x and λ_t represent the flow length and times scales. The results are consistent with the findings of an earlier assessment by de Kat and van Oudheusden (2012). It was found that depending on the numerical implementation employed, flow structures with a small turnover time with respect to the (pseudo-)track length (i.e. large $\Delta T/\lambda_t$) may appear as small-scale artefacts in the calculated material acceleration and pressure fields. Further, it was concluded that when considering the energy spectrum associated with the convection of a flow structure evaluated at a fixed point in space, no meaningful contributions to the energy content can be expected for frequencies above $f_c = 0.2U_c/\text{WS}$ and from flow structures for which $\Delta T/\lambda_t > 0.2$ or $\text{WS}/\lambda_x > 0.2$.

For the experimental assessment, pressure fields have been calculated from time-resolved tomographic PIV measurements. Reference pressure data at the model surface have been obtained by microphones and via static pressure taps. Depending on the track length used in the pseudo-tracking method, the PIV-based pressure and reference measurements showed a fair agreement in terms of mean levels, fluctuation levels and energy content in frequency spectra. The coherence and correlation between microphone and PIV pressure measurements were found to be substantial and indicated that the low-frequency pressure development in the flow can be reproduced regardless of the (pseudo-)track length used. Supporting the outcome of the theoretical/numerical assessment, pressure wavelength spectra suggested a cut-off wavelength of $\text{WS}/\lambda_x = 0.2$, while pressure frequency spectra suggested a cut-off frequency of $\Delta T/\lambda_t = 0.2$, based on a threshold of -3 dB.

Based on the results of a spectral analysis, a method was proposed to inform the selection of a suitable (pseudo-)track length as well as to estimate the local error margin of PIV-based pressure values. The method makes use of experimental data only and does not require the availability of any reference data.

Acknowledgments

This work is supported by the European FP-7 project NIOPLEX, grant agreement 605151. The measurements used in the experimental assessment were performed in collaboration with Valeria Gentile.

Appendix. Microphone calibration procedure

Inspired by Wong (2014), the gain and phased shift of each microphone-pinhole-amplifier combination as a function of frequency is obtained by calibration against a reference microphone. The response of the measurement microphone with respect to the reference microphone is used to correct the measured signals as a means of deconvolution. The procedure consists of the followings steps. Specifics for the presents study are included between brackets:

(i) The reference microphone (the type LinearX M53 ($\frac{1}{4}$-inch diameter, nominal sensitivity of 140 mV/94dBSPL) is calibrated by measuring its response to a signal with a known amplitude (a 250 Hz signal from a G.R.A.S. 42AA pistonphone). The reference sensitivity is combined with the frequency response curve specified by the manufacturer.

(ii) A acoustical coupler (custom-made, 2cc) is placed over a pinhole in the model that holds the measurement microphone. A rubber pad is used to ensure airtight sealing. The reference microphone is mounted on the top of the coupler and a speaker is mounted halfway in the side-wall. The speaker is set to generate a white noise signal (103 dB).

(iii) The frequency response in terms of gain and phase shift of the measurement microphone versus the reference microphone is taken as the cross power spectral density estimate of the signals from both microphones. Spectral noise can be reduced by breaking the signal in segments and averaging the frequency spectra of windowed segments, e.g. Welch's method. Note that the individual segments need to be long enough to be able to contain the lowest frequency of interest. Alternatively or in addition, the gain and phase shift can be smoothed using a moving average filter (the present study used both approaches resulting in a spectral resolution of 2 Hz). Note that since high spectral noise can result from poor microphone mounting, smoothness of the frequency response also serves as a quality indicator of the measurement. Other potential causes of a non-smooth frequency response include lack of statistical convergence, the use of non-perfect white noise and the presence of resonance frequencies.

(iv) The gain and phase shift of the measurement microphone is obtained by multiplying the frequency response from step 3 with the frequency response curve of the reference microphone from step 1.

(v) The resulting frequency response can be cut-off to incorporate a low-pass, high-pass or band-pass filter (in the present case, the response is cut off at $\mathrm{St}_D = 0.1$ (20 Hz) and $\mathrm{St}_D = 1.0$ (200 Hz) to include a band-pass filter).

(vi) The cut-off response is converted to the time-domain by taking the inverse discrete Fourier transform and conditioned, i.e. shifted, truncated and windowed. The response is then again moved back to the frequency domain to obtain a filter kernel.

(vii) Measurements are corrected by taking its discrete Fourier transform, multiplying the resulting frequency-representation with the filter kernel, and taking the inverse discrete Fourier transform to obtain the corrected time-representation.

(viii) The procedure is validated by checking that after applying it, the corrected calibration signal from the measurement microphone collapses with the calibration signal from the reference microphone.

ORCID iDs

P L van Gent https://orcid.org/0000-0001-9972-1681

References

Atkinson C and Soria J 2009 An efficient simultaneous reconstruction technique for tomographic particle image velocimetry *Exp. Fluids* **47** 553–68

Butz T *Fourier Transformation for Pedestrians (Undergraduate Lecture Notes in Physics*) 2nd edn (Berlin: Springer)

Charonko J J, King C V, Smith B L and Vlachos P P 2010 Assessment of pressure field calculations from particle image velocimetry measurements *Meas. Sci. Technol.* **21** 105401

de Kat R and van Oudheusden B W 2012 Instantaneous planar pressure determination from PIV in turbulent flow *Exp. Fluids* **52** 1089–106

Deck S and Thorigny P 2007 Unsteadiness of an axisymmetric separating-reattaching flow: numerical investigation *Phys. Fluids* **19** 065103

Discetti S and Astarita T 2012 Fast 3D PIV with direct sparse cross-correlations *Exp. Fluids* **53** 1437–51

Discetti S, Natale A and Astarita T 2013 Spatial filtering improved tomographic PIV *Exp. Fluids* **54** 1505

Foucaut J M and Stanislas M 2002 Some considerations on the accuracy and frequency response of some derivative filters applied to particle image velocimetry vector fields *Meas. Sci. Technol.* **13** 1058–71

Foucaut J M, Carlier J and Stanislas M 2004 PIV optimization for the study of turbulent flow using spectral analysis *Meas. Sci. Technol.* **15** 1046–58

Gentile V, Schrijer F, van Oudheusden B and Scarano F 2016 Afterbody Effects on Axisymmetric Base Flows *53rd AIAA Aerospace Sciences Meeting (AIAA SciTech Reston, Virginia American Institute of Aeronautics and Astronautics)*

Gorry P 1990 General least-squares smoothing and differentiation by the convolution method *Anal. Chem.* **62** 570–3

Jensen A and Pedersen G K 2004 Optimization of acceleration measurements using PIV *Meas. Sci. Technol.* **15** 2275–83

Jensen A, Pedersen G K and Wood D J 2003 An experimental study of wave run-up at a steep beach *J. Fluid Mech.* **486** 161–88
Jeon Y J, Chatellier L, Beaudoin A and David L 2015 Least-square reconstruction of instantaneous pressure field around a body based on a directly acquired material acceleration in time-resolved PIV *11th Int. Symp. on Particle Image Velocimetry (Santa Barbara, CA)*
Laskari A, de Kat R and Ganapathisubramani B 2016 Full-field pressure from snapshot and time-resolved volumetric PIV *Exp. Fluids* **57** 44
LaVision 2015 Product-manual for DaVis 8.3
Liu X and Katz J 2006 Instantaneous pressure and material acceleration measurements using a four-exposure PIV system *Exp. Fluids* **41** 227–40
Liu X and Katz J 2013 Vortex-corner interactions in a cavity shear layer elucidated by time-resolved measurements of the pressure field *J. Fluid Mech.* **728** 417–57
Lynch K P and Scarano F 2014a Experimental determination of tomographic PIV accuracy by a 12-camera system *Meas. Sci. Technol.* **25** 084003
Lynch K P and Scarano F 2014b Material acceleration estimation by four-pulse tomo-PIV *Meas. Sci. Technol.* **25** 084005
Lynch K, Pröbsting S and Scarano F 2014 Temporal resolution of time-resolved tomographic PIV in turbulent boundary layers *17th Int. Symp. on Applications of Laser Techniques to Fluid Mechanics (Lisbon)*
McClure J and Yarusevych S 2017 Optimization of planar PIV-based pressure estimates in laminar and turbulent wakes *Exp. Fluids* **58** 62
Panton R 1996 *Incompressibe Flow* (New York: Wiley)
Pope S B 2000 *Turbulent Flows* (Cambridge: Cambridge University Press)
Scarano F and Poelma C 2009 Three-dimensional vorticity patterns of cylinder wakes *Exp. Fluids* **47** 69–83
Scarano F and Riethmuller M L 2000 Advances in iterative multigrid PIV image processing *Exp. Fluids* **29** S051–60
Schiavazzi D, Coletti F, Iaccarino G and Eaton J K 2014 A matching pursuit approach to solenoidal filtering of three-dimensional velocity measurements *J. Comput. Phys.* **263** 206–21
Schrijer F F J and Scarano F 2008 Effect of predictor-corrector filtering on the stability and spatial resolution of iterative PIV interrogation *Exp. Fluids* **45** 927–41
Shaw R 1960 The influence of hole dimensions on static pressure measurements *J. Fluid Mech.* **7** 550–64
Theunissen R 2012 Theoretical analysis of direct and phase-filtered cross-correlation response to a sinusoidal displacement for PIV image processing *Meas. Sci. Technol.* **23** 065302
Thomas L, Vernet R, Tremblais B and David L 2010 Influence of geometric parameters and image preprocessing on tomo-PIV results *15th Int. Symp. on Apllications of Laser Techinques to Fluid Mechanics (Lisbon)*
van Gent P L *et al* 2017 Comparative assessment of pressure field reconstructions from particle image velocimetry measurements and Lagrangian particle tracking *Exp. Fluids* **58** 33
van Gent P, Schrijer F F J and van Oudheusden B W 2018 Assessment of the pseudo-tracking approach for the calculation of material acceleration and pressure fields from time-resolved PIV: part I. Error propagation *Meas. Sci. Technol.* **29** 045204
van Oudheusden B W 2013 PIV-based pressure measurement *Meas. Sci. Technol.* **24** 032001
Violato D, Moore P and Scarano F 2011 Lagrangian and Eulerian pressure field evaluation of rod-airfoil flow from time-resolved tomographic PIV *Exp. Fluids* **50** 1057–70
Weiss P E, Deck S, Robinet J C and Sagaut P 2009 On the dynamics of axisymmetric turbulent separating/reattaching flows *Phys. Fluids* **21** 075103
Westerweel J and Scarano F 2005 Universal outlier detection for PIV data *Exp. Fluids* **39** 1096–100
Wieneke B 2008 Volume self-calibration for 3D particle image velocimetry *Exp. Fluids* **45** 549–56
Wong G S 2014 *Microphones and Their Calibration* ed T Rossing(*Springer Handbook of Acoustics*) (Berlin: Springer) Part H